

Cite this: DOI: 00.0000/xxxxxxxxxx

Bouncing-to-wetting transition for impact of water droplets on soft solids

Surjyasish Mitra ^a, Quoc Vo ^{b,*}, and Tuan Tran ^{b,**}Received Date
Accepted Date

DOI: 00.0000/xxxxxxxxxx

Soft surfaces impacted by liquid droplets trap more air underneath than their rigid counterpart. The extended lifetime of the air film not only facilitates bouncing behaviours of the impacting droplets but also increases the possibility of an interaction between the air film itself and the air cavity formed inside the droplets by capillary waves. Such interaction may cause rupture of the trapped air film by a so-called dimple inversion phenomenon and suppress bouncing. In this work, we systematically investigate the relation between air cavity collapse and air film rupture for water droplets impacting on soft, hydrophobic surfaces. By constructing a bouncing-to-wetting phase diagram based on the rupturing dynamics of the trapped air film, we observe that the regime in which air film rupture is induced by dimple inversion consistently separates the bouncing regime and the one in which wetting is caused by random rupture. We also find that air film rupture by dimple inversion, in-turn, affects both the collapsing dynamics of the air cavity and the resulting high-speed jet. We then provide a detailed characterisation of the collapsing dynamics of the air cavity and subsequent jetting.

1 Introduction

The air film separating an impacting liquid droplet with an impacted surface plays a crucial role in dictating impact outcomes. For high velocity impacts, the lubrication pressure built-up in the air film causes liquid splashes^{1,2}. For low velocity impacts, the presence of a sustained air film leads to bouncing of the droplets regardless of surface's wettability³⁻⁷. Studies of the bouncing-to-wetting transition of low velocity water droplets impacting on solid surfaces are motivated by both fundamental and practical interests. The former motivation comes from numerous intangible physical phenomena, e.g., capillary waves⁸, air entrapment dynamics⁵, involved in dictating such transition, while the latter one is from applications requiring design of dynamic surfaces such as anti-bacterial, self-cleaning surfaces⁹ or improvement of industrial processes including droplet deposition¹⁰ and ink-jet printing¹¹. Although numerous investigations have been focusing on the bouncing-to-wetting transition, in particular on the dynamics of the intervening air film at the moment wetting occurs^{3-7,12}, the mechanisms causing such transition remains elusive.

Typically, the prelude to the final touchdown between an approaching droplet and a solid surface is the formation of a thin air film in which lubrication pressure is built up. The lubrication pressure subsequently becomes sufficiently large that it de-

forms the droplet's bottom surface, creating a central dimple surrounded by an outer edge with one or two kinks, the regions where the air film thickness is minimum^{5,6,13}. For impact on hydrophilic surfaces, bouncing is ensured at low impact velocity. For higher impact velocity, the air film typically ruptures either at inner or outer kink leading to wetting initiation^{5,6}. In other words, bouncing-to-wetting transition for droplets impacting smooth hydrophilic surfaces, e.g., glass or mica, is mainly determined by air film's dynamics and the surface properties that cause random wetting initiation^{5,6}.

Impact outcomes on soft surfaces are markedly different¹⁴⁻¹⁶. On the one hand, an elastomer or gel coated surface is usually hydrophobic¹⁷. Thus, impacts of water droplets on such soft surfaces appear to have characteristics similar to those on smooth, rigid hydrophobic surfaces^{18,19}. An impacting droplet above a critical impact velocity may develop a pyramidal structure due to capillary waves induced upon impact. This leads to formation of a cylindrical air cavity that penetrates deeply into the droplet and eventually collapses, shooting out a liquid jet^{14,15,18,19}. On the other hand, due to the deformation of the soft solids, air film trapped beneath the impacting droplets have a longer lifetime compared to those impacting on a rigid one¹⁶. The sustained air film not only inhibits wetting initiation and facilitates bouncing of the impacting droplet^{14,15}, but also increases the probability for interaction between the air film and the air cavity formed in the liquid bulk. We note that the latter condition is rarely met for impacts on smooth, rigid hydrophilic or hydrophobic surfaces due to random air film rupture and wetting initiation^{5,6,18,19}. Whether the interactions between the trapped air film and the air

^a School of Physical & Mathematical Sciences, Nanyang Technological University, 50 Nanyang Avenue, 639798 Singapore

^b School of Mechanical & Aerospace Engineering, Nanyang Technological University, 50 Nanyang Avenue, 639798 Singapore. E-mail: * xqvo@ntu.edu.sg, ** tran@ntu.edu.sg

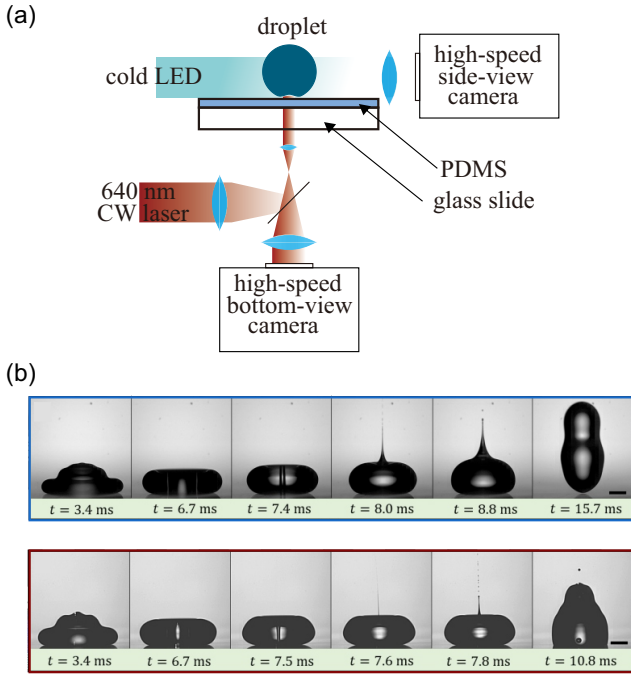


Fig. 1 (a) Schematic of the experimental setup. (b) Impact dynamics of a 1.16 mm water droplet on soft PDMS 60:1 substrates with Young's modulus $E = 4.8\text{ kPa}$ and two impact velocities: 0.33 ms^{-1} ($We = 1.7$) (upper panel), 0.39 ms^{-1} ($We = 2.4$) (lower panel). The snapshots corresponding to the last column in both panels show two different impact outcomes: bouncing and deposition with entrapped air bubble. Scale bars represent 0.5 mm.

cavity dictates the wetting initiating mechanism of the bouncing-to-wetting transition for impact of water droplets on soft surfaces remains an open question.

In this work, we experimentally study the bouncing-to-wetting transition of water droplets impacting on soft surfaces. We hypothesise that such transition is determined by interactions between the air cavity and the air film trapped beneath the impacting droplets. To test this hypothesis, we first use both high-speed laser interferometry and high-speed optical imaging to characterize the rupture mechanism of the air film and the dynamics of the air cavity in the bulk. We reveal how interaction between the air film and the cavity's collapsing dynamics results in different types of air film rupture. We then construct a phase diagram describing the dependence of the bouncing-to-wetting transition on the stiffness of the substrate and the impact characteristics based on the characterized air film rupture mechanisms. Finally, we provide an explanation for the collapsing dynamics of the air cavity and the resulting high-speed jets and bubble entrapment.

2 Experiments

Our test substrates were glass slides coated with a layer of Polydimethylsiloxane (PDMS) of thickness $70\text{ }\mu\text{m}$. The elasticity E of the substrate was varied from 4.8 kPa to 263.6 kPa by changing the ratio of the monomer to crosslinker from 60:1 to 30:1 (Tab. 1). The equilibrium contact angle θ_Y of a small water droplet on the test substrates varied between 103.6° and 113.0° (Tab. 1). Im-

portant experiments were conducted using water droplets with radius r_0 varying from 0.63 mm to 1.4 mm ; the velocity v of the impacting droplets was varied between 0.30 ms^{-1} and 0.51 ms^{-1} . The Weber number, defined as $We = \rho r_0 v^2 / \gamma$, thus varies from 2.1 to 5.1. Here, $\rho = 1000\text{ kg m}^{-3}$ and $\gamma = 72\text{ Nm}^{-1}$ respectively are the density and surface tension of water.

Impacting droplets were recorded synchronously from the bottom and the side using two high-speed cameras (SA-X2 and SA-5, Photron) operating at imaging rates from 30,000 to 200,000 frames-per-second and shutter time $1/800,000$. This setup has a temporal resolution at $3.75\text{ }\mu\text{s}$. A cold LED light source was used for side view illumination, while a red diode laser (wavelength $\lambda = 640\text{ nm}$) was used to illuminate the impacted surface from below (Fig. 1a). The laser illumination coupled with a $5\times$ optical zoom lens enabled us to observe the dimple profile with a height resolution of $\lambda/4 = 160\text{ nm}$ ^{6,20}, and a horizontal resolution of $3.5\text{ }\mu\text{m/pixel}$.

3 Results and Discussions

3.1 Bouncing-to-wetting transition

For impacts of low viscosity liquids, the intrinsic length scale of the capillary waves induced upon impact is the wavelength $\lambda_c \sim \gamma \rho^{-1} v^{-2}$ ¹⁸. The condition for capillary wave formation is $\lambda_c > r_0$, or equivalently $We > 1$. As the Weber number in our experiment varies between 2 and 5, both inertial and capillary forces are significant. In this Weber number range, impacting droplets deform into pyramidal shapes, as shown in Fig. 1b ($t = 3.4\text{ ms}$).

From side-view images, we observe two distinct macroscopic behaviours when the velocity v of the impacting droplet increases: the droplet either bounces off from the substrate at low impact velocity (Fig. 1b, upper panel) or is deposited onto the substrate as the impact velocity is increased (Fig. 1b, lower panel). In both cases, we observe that the air cavity forms roughly at the moment the droplet reaches the maximum deformation and starts retracting (Fig. 1b, $t = 6.7\text{ ms}$). Subsequently, the air cavity collapses resulting in liquid jets from the droplet. Typically, we observe that the jet velocity is higher in the case of depositing droplets compared to that of bouncing droplets from the substrate.

To reveal mechanisms causing the different impact outcomes, i.e., bouncing or deposition, in Fig. 2, we show bottom-view interferometric recordings and the corresponding extracted profiles of the air film trapped between the liquid and the solid upon impact. In all cases, the liquid droplet initially skates on a thin film of air with the bottom liquid-air interface expanding at a lateral speed $\sim 0.2\text{ ms}^{-1}$, in close proximity to those reported in a recent study for impacts in a similar range of Weber number²¹. While expanding, the bottom surface of the droplet deforms into the familiar dimple profile^{4,6} with two distinct kinks due to excess pressure in the trapped air film, evident from the recorded interference signatures (see Fig. 2 a-d, $t = 0.34\text{ ms}$).

The evolution of the trapped air film is sensitive to the impact velocity. At low impact velocity, $v \leq 0.36\text{ ms}^{-1}$ (Fig. 2a), the air film remains intact during the entire duration of impact. Therefore, the droplet bounces off from the substrate similar to pre-

Table 1 Substrates used in our experiments. The numbers show the weight ratio of the monomer to crosslinker. The value of stiffness E is measured experimentally using a rheometer. Equilibrium contact angles are measured using the sessile drop technique.

Substrates:	P60:1	P50:1	P40:1	P35:1	P30:1
E (kPa)	4.8	29.5	70.9	142.7	263.6
θ_Y	$109.5^\circ \pm 3.5^\circ$	$108.2^\circ \pm 1.7^\circ$	$107.7^\circ \pm 0.8^\circ$	$107.0^\circ \pm 1.3^\circ$	$106.8^\circ \pm 3.2^\circ$

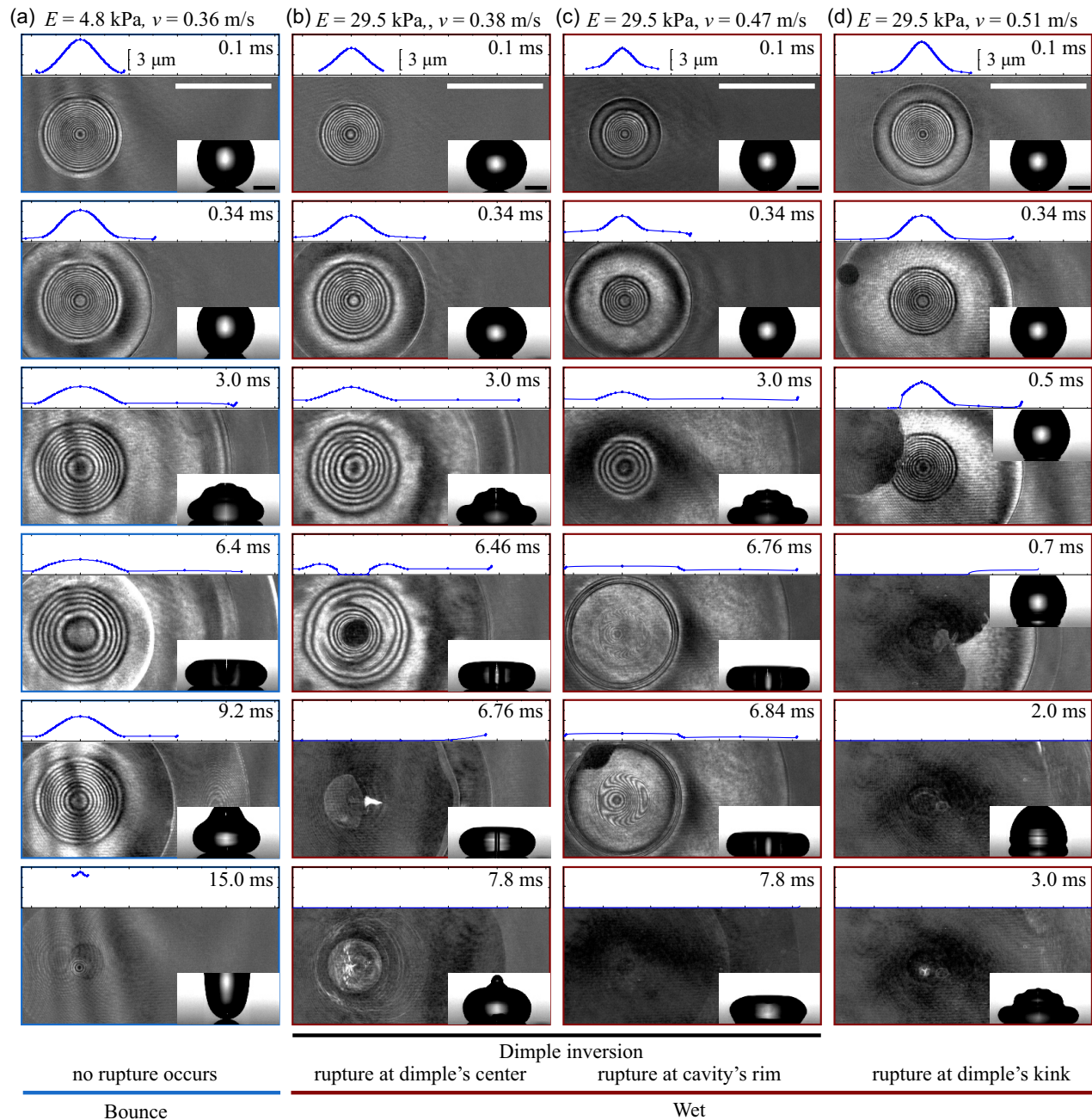


Fig. 2 Air film rupture dynamics of 1.4 mm radius water drops impacting on soft PDMS surfaces at different impact velocity v . (a) At $v = 0.36 \text{ ms}^{-1}$, the droplet bounces after impact without wetting the solid surface. (b) At $v = 0.38 \text{ ms}^{-1}$, a perfect inversion of the air cavity causes rupture of the air film at the dimple's center. Liquid jet and air bubble entrapment caused by the collapse of air cavity are observed. (c) At $v = 0.47 \text{ ms}^{-1}$, rupture of air film occurs at the rim of the air cavity. (d) At $v = 0.51 \text{ ms}^{-1}$, rupture of air film occurs randomly at the rim location where the air film is thinnest. The scale bars in both side-view and bottom-view images represent 1 mm.

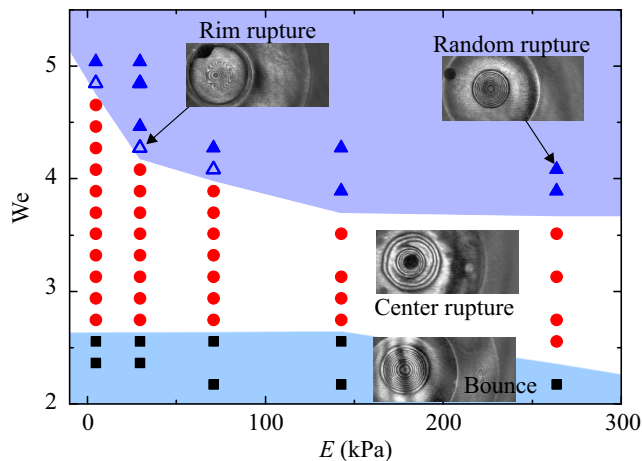


Fig. 3 Phase diagram showing the general behaviours, i.e., bouncing, dimple inversion and wetting, of droplets impacting on soft solid. The behaviours are obtained by varying Weber number We and Young modulus E of the soft substrates. The droplet is water having fixed radii $r_0 = 1.4$ mm.

vious studies involving droplet bouncing on glass⁵ and PDMS¹⁵ surfaces. For $0.38 \text{ ms}^{-1} \leq v \leq 0.47 \text{ ms}^{-1}$, the air cavity in the bulk forces the dimple downward causing shape inversion. The air film separating the inverted dimple and the soft solid eventually ruptures, initiating wetting. We observe two distinct types of wetting initiation caused by the inversion of the dimple: wetting either first occurs at the center of the dimple (Fig. 2b, $t = 6.76$ ms), or at the dimple's inner rim (Fig. 2c, $t = 6.84$ ms). While wetting initiation at dimple's center had been previously observed in a similar study of droplet impact on PDMS surfaces¹⁴, wetting initiation at dimple's inner rim due to dimple inversion has not been reported. In our experiment, the wetting initiation at the dimple's inner rim consistently happens at impact velocity slightly higher than that at the dimple's center. For a higher range of impact velocity, $v \geq 0.51 \text{ ms}^{-1}$, rupture of the air film initiates at a random position near the inner or outer kink (Fig. 2d, $t = 0.34$ ms) consistent with previous drop impact studies on rigid and soft surfaces^{4,6,15}.

In Fig. 3, we show a phase diagram presenting how the Weber number We and surface elasticity E affect the behaviour of the trapped air film and the resulting impact outcomes. Generally, we observe that dimple inversion causing air film rupture at the center of the dimple is sandwiched between two other major behaviours: bouncing and random rupture. Wetting initiated by rupture at the dimple's rim (open triangles) appears as a transitional behaviour separating the center rupture and the random rupture behaviours. In other words, for a fixed soft substrate, increasing the We number causes the impact dynamics to change from bouncing to center rupture, rim rupture and finally random rupture. For surfaces with $E > 142$ kPa, we do not observe the rim rupture behaviour. We also observe that increasing the substrate elasticity E , while causing insignificant effect to the transition between bouncing and wetting considerably reduces the transitional We number between center rupture and rim rupture. This is qualitatively consistent with the fact that increasing the surface

stiffness results in less air entrapment and thinner air film, which eventually leads to random rupture of the air film and wetting initiation^{5,6}.

3.2 Collapse dynamics of air cavity

The dimple and air film dynamics not only affect the general impact outcomes but also alter the formation and collapse of the air cavity formed upon impact. In Fig. 4, we show several series of snapshots highlighting the formation and collapse of the air cavity upon impact of $r_0 = 1.4$ mm water droplets on soft PDMS surfaces having $E = 70.9$ kPa. At low impact velocity, i.e., $v = 0.33 \text{ ms}^{-1}$, we observe that a U-shaped cavity is partially formed (Fig. 4a). Subsequently, the droplet's surface restores to its minimum surface area pushing the cavity out. No liquid jet or air bubble entrapment inside the liquid bulk is observed. At $v \geq 0.36 \text{ ms}^{-1}$, the capillary waves on the droplet's surface are sufficiently strong to form a cylindrical cavity through the droplet width (Fig. 4b-f, the first snapshots). Subsequently the cavity radius retracts and eventually collapses resulting in liquid jet and bubble entrapment. Depending on the impact velocity v , the cavity either collapses at the bottom of the cylindrical cavity (Fig. 4b, $t = 7.36$ ms), or at the cavity's waist (Fig. 4c, $t = 6.82$ ms), cavity's top (Fig. 4d, $t = 7.16$ ms) or at both top and bottom (Fig. 4e, $t = 7.60$ ms). We attribute the different collapsing dynamics of the cavity to the capillary waves on the cavity surface which is clearly observed in (Fig. 4b-e): the collapse position occurs at the wave's peak. At high impact velocity, where the air film ruptures randomly, (Fig. 4f), the wetting initiation at the rupture point disturbs the retracting cavity in the bulk.

Interestingly, we observe that the relative temporal order between wetting initiation and complete collapse of the air cavity depends on both impact velocity and droplet radius. As shown in Fig. 4c-e, with a fixed droplet radius ($r_0 = 1.4$ mm), the duration $t_c - t_r$ decreases from 0.36 ms to 0 ms when the impact velocity v increases from 0.38 ms^{-1} (Fig. 4c) to 0.45 ms^{-1} (Fig. 4e). Here, t_r is the moment at which rupture by dimple inversion happens (dashed-blue boxes in Fig. 4). In Fig. 5, we show that wetting occurs *before* the final collapse of the air cavity for larger droplets (see Fig. 5a, $r_0 = 1.4$ mm) and *after* the collapse of the air cavity for smaller droplets (see Fig. 5c, $r_0 = 0.63$ mm). The radius at which the temporal order between wetting initiation and cavity collapse switches is $r_0 = 1.16$ mm (Fig. 5b). This is consistent with a previously reported experimental observation by Chen et al.¹⁴ in which wetting initiation at the dimple center occurs after the air cavity completely collapses for water droplets of radius $r_0 = 1$ mm and a similar Weber number impacting on PDMS coated substrates.

To quantitatively characterize the collapsing dynamics of the air cavity, we measure the evolution of the retracting cavity radius r_c . In Fig. 6, we show the dependence of r_c on $t_c - t$ for different impact outcomes, i.e., bounce or wet, while varying the surface elasticity E , droplet radius r_0 , and impact velocity v . Here, r_c is the cavity radius measured along the location where the air cavity eventually collapses, t_c the time instant when the retracting cavity completely collapses. It should be noted here that we only

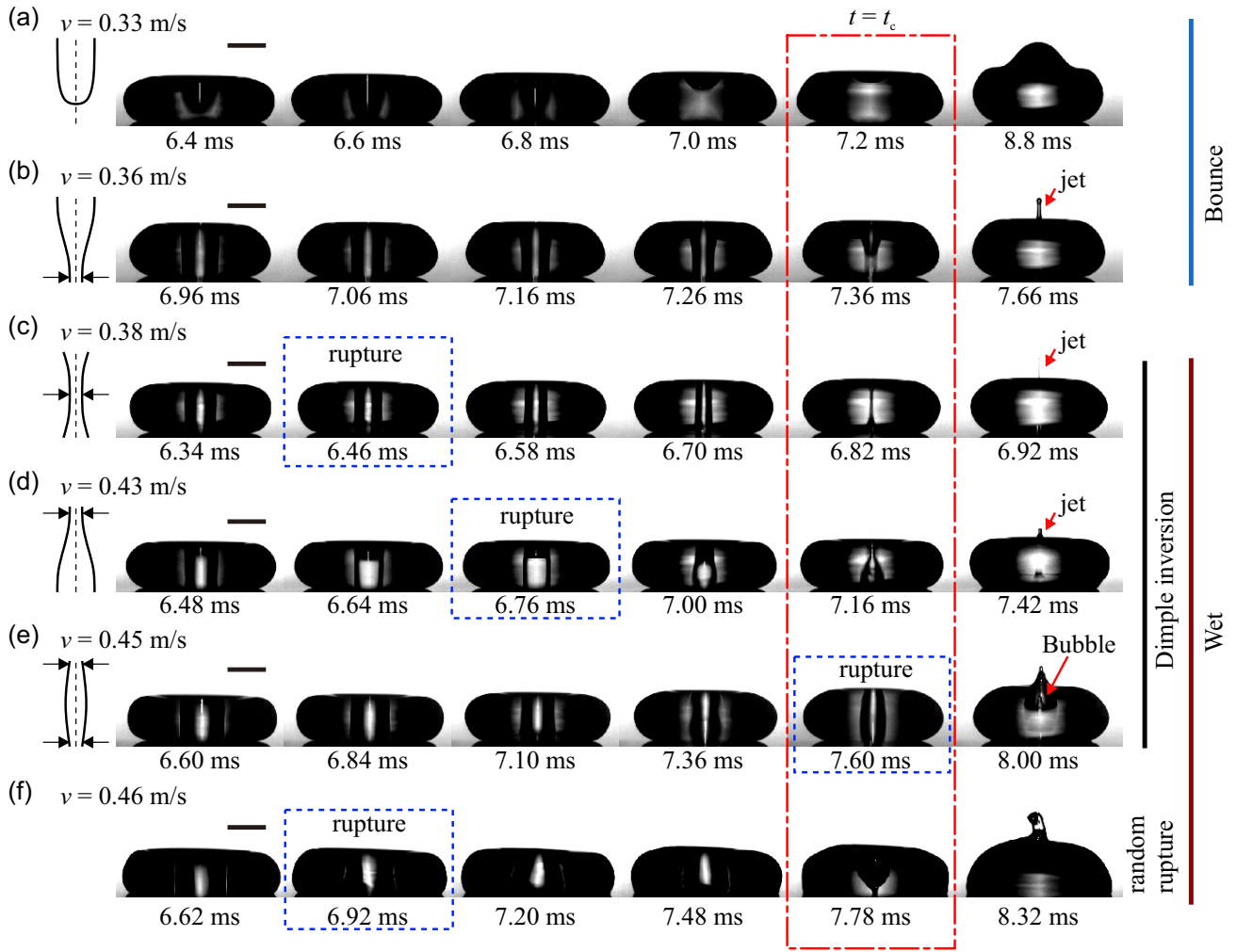


Fig. 4 Snapshots showing the formation and collapse of air cavity during impacts of $r_0 = 1.4$ mm water droplets onto PDMS 40:1 substrates with $E = 70.9$ kPa at different impact velocities v . From (a) to (f), the impact velocity v increases from 0.33 m/s to 0.46 m/s resulting in different collapse dynamics of the air cavity. The dashed boxes show the snapshots at the moment the air film ruptures. The schematics show the air cavity shapes right before collapse, i.e., $t = t_c$ (see the dashed-dotted box). The arrows in each schematic show the position where the collapse occurs. In all cases, the scale bars represent 1 mm.

show values of r_c measured in the case that the air cavity symmetrically collapses, which case occurs when the droplets bounces or wet the substrate by dimple inversion (Fig. 4b-e). In the case that random rupture occurs, it is not possible to accurately measure r_c as the cavity collapses asymmetrically (Fig. 4f). We observe two distinct collapsing behaviours depending on the impact outcomes: $r_c \sim (t_c - t)^{1/2}$ for bouncing droplets (Fig. 6a,b), and $r_c \sim (t_c - t)^{2/3}$ for wetting induced by dimple inversion (Fig. 6c,d). We observe that elasticity of the substrate E does not affect the dependence of r_c on $t_c - t$ in both bouncing and dimple inversion regimes. In other words, although surface elasticity significantly affects the transition between bouncing and dimple inversion, the formation and collapse of the air cavity is mainly determined by the hydrodynamical properties of the droplets.

For impacts in the bouncing regime (Figs. 2a and 4a,b), it was shown in previous studies^{18,19,22} that the air cavity's dynamics is dominated by inertia, leading to the relation $r_c \sim (\gamma r_0)^{1/4} \rho^{-1/4} (t_c - t)^{1/2}$. This is indeed consistent with the power

law $r_c \sim A(t_c - t)^{1/2}$ observed in our experiment (Fig. 6a,b). Fitting this power law to our experimental data collected for r_0 in the range from 0.63 mm to 1.4 mm respectively yields A from 0.010 to 0.022 consistent with the calculated values of $(\gamma r_0)^{1/4} \rho^{-1/4}$ from 0.014 to 0.020.

For impacts in which the air film ruptures due to dimple inversion, we observe a different power-law behaviour for the collapsing cavity radius. We argue that the fast contact line motion at the rupture point generates capillary waves on the cavity's surface (Fig. 4); these waves act as the driving factor for the subsequent collapse of the cavity. As the collapsing dynamics is in the inertial regime, the capillary waves are self-similar with phase velocity $u \sim \gamma^{1/3} [\rho(t_c - t)]^{-1/3}$ ²³⁻²⁶ in the present context. Consequently, balancing the dynamical pressure ρu^2 with the Laplace pressure γr_c^{-1} at the collapsing position results in an expression for retract-

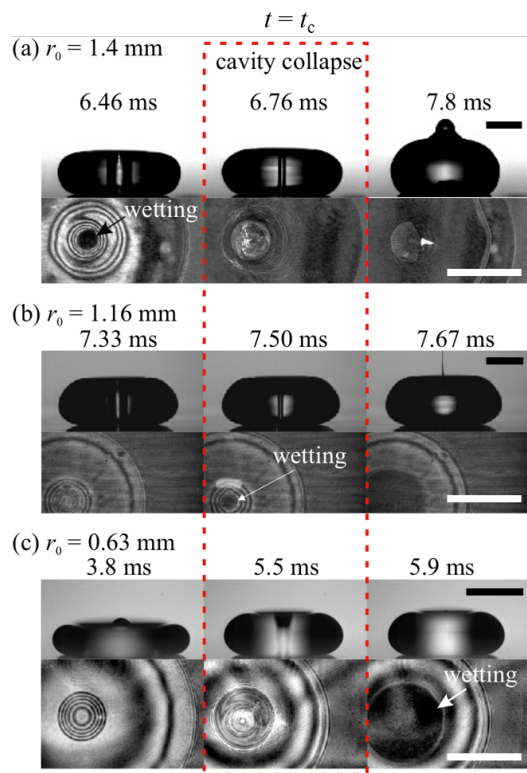


Fig. 5 Snapshots showing changes in temporal order of air cavity collapse and wetting initiation by varying droplet radius: (a) $r_0 = 1.4\text{ mm}$, wetting occurs before cavity collapse; (b) $r_0 = 1.16\text{ mm}$, wetting initiates right at the moment cavity collapses; (c) $r_0 = 0.63\text{ mm}$, wetting initiates after cavity completely collapsed. Parameters: (a) $E = 29.5\text{ kPa}$, $We = 2.8$; (b) $E = 4.8\text{ kPa}$, $We = 2.4$; (c) $E = 4.8\text{ kPa}$, $We = 2.3$. Scale bars in both the side-view and bottom-view snapshots represent 1 mm.

ing cavity radius:

$$r_c \sim \left(\frac{\gamma}{\rho}\right)^{1/3} (t_c - t)^{2/3}. \quad (1)$$

Eq. 1 indicates that the dependence of r_c on $t_c - t$ in the case that dimple inversion happens does not depend on either droplet radius r_0 or the impact velocity v , consistent with our experimental data shown in Fig. 6d.

3.3 Liquid jet dynamics

When the air cavity collapses due to necking, it is divided into two air cavities which subsequently evolve differently under surface tension effects. On one hand, the enclosed geometry of the lower air cavity prevents the air from escaping and eventually results in an air bubble entrapped inside the liquid bulk. On the other hand, the upper air cavity, which is connected to the ambient air at its top continues to collapse and finally generates a liquid jet as illustrated in Fig. 1b. As a result, the jetting dynamics, i.e., the jet's radius and velocity, strongly depends on the collapsing dynamics of the air cavity.

In Fig. 7a and b, we show two different jetting dynamics as a result of air cavity collapse dynamics, i.e., cylindrical cavity

(Fig. 4c) or conical cavity (Fig. 4b, d). When jetting is induced by cylindrical air cavity collapse, we observe that the jets have small radius and high velocity (Fig. 7a). The jet's shape does not depend on whether the droplets bounce or wet the solid. However, we observe that the jetting velocity is much higher when the droplets wet the solid by dimple inversion compared to that when it bounces. For wetting by dimple inversion, we observe jet velocity as high as 37 m s^{-1} . Whereas, for bouncing scenarios, the jet velocity observed is typically in the range $2\text{ m s}^{-1} - 10\text{ m s}^{-1}$. When the air cavity collapses at its ends, the so-called conical collapse (Fig. 7b), the jets have larger radius and lower velocity compared to those of the cylindrical collapse. Typical jet velocity for conical collapse is approximately 2 m s^{-1} . Whether the air film ruptures or not does not significantly affect either the radius or velocity of the jets. The maximum jet velocity observed in our experiments is approximately 100 times the impact velocity. This is higher than the maximum jet velocity of droplets impact on hydrophilic, hydrophobic, or superhydrophobic surfaces reported in previous studies^{18,19,27-29}, i.e., 16 – 55 times the impact velocity. We note that the lower bound of jet velocity in our case, i.e., approximately 1 m s^{-1} is similar to those observed in the mentioned studies^{18,19,27-29}. The jet velocity appears to be more dependent on the nature of air cavity at collapse, i.e., conical or cylindrical, rather than the elasticity of the soft surfaces or their hydrophobic character.

For the lower air cavity which fails to escape, we consistently observe that it eventually gets trapped inside the liquid bulk as an air bubble. From our experiments, we find the radius of the entrapped air bubble to vary between $100\text{ }\mu\text{m} - 400\text{ }\mu\text{m}$. The entrapped air bubble freely floats around in the liquid bulk.

In Fig. 7c, we show snapshots of a special case in which a thin liquid jet emanates from the bottom of the retracting air cavity and shoots upwards ($t \geq 7.8\text{ ms}$) after wetting initiates at the center due to dimple inversion ($t = 7.48\text{ ms}$). This jet is similar to the one reported by Chen et al.¹⁹ for impacting of droplets on structured PDMS surfaces. We note here that the onset of the jet occurs approximately 0.30 – 0.35 ms after air film rupture and wetting initiation suggesting that the jet directly links to dimple inversion causing air film rupture at the impact center. Typically, the jet radius varies between $15\text{ }\mu\text{m}$ and $45\text{ }\mu\text{m}$. It appears that the liquid jet expands radially briefly, for a duration of $60\text{ }\mu\text{s} - 80\text{ }\mu\text{s}$, before terminating into tiny droplets. The liquid jetting is immediately followed by air cavity collapse and its accompanying jet. Hence, for such impact scenarios, we observe jets from both thin liquid film collapse and air cavity collapse.

4 Concluding remarks

In summary, we have experimentally investigated the impact characteristics of water droplets on soft PDMS surfaces at low velocity. We observed that soft surfaces promotes bouncing for a higher range of impact Weber number as compared to smooth hydrophilic or hydrophobic surfaces^{5,6}. Further, using interference, we probed the interaction between the collapsing air cavity in the bulk of an impacting droplet and the air film separating the droplet with the impacted soft surface. Above a threshold impact velocity, the interaction induces inversion of the dimple in the air

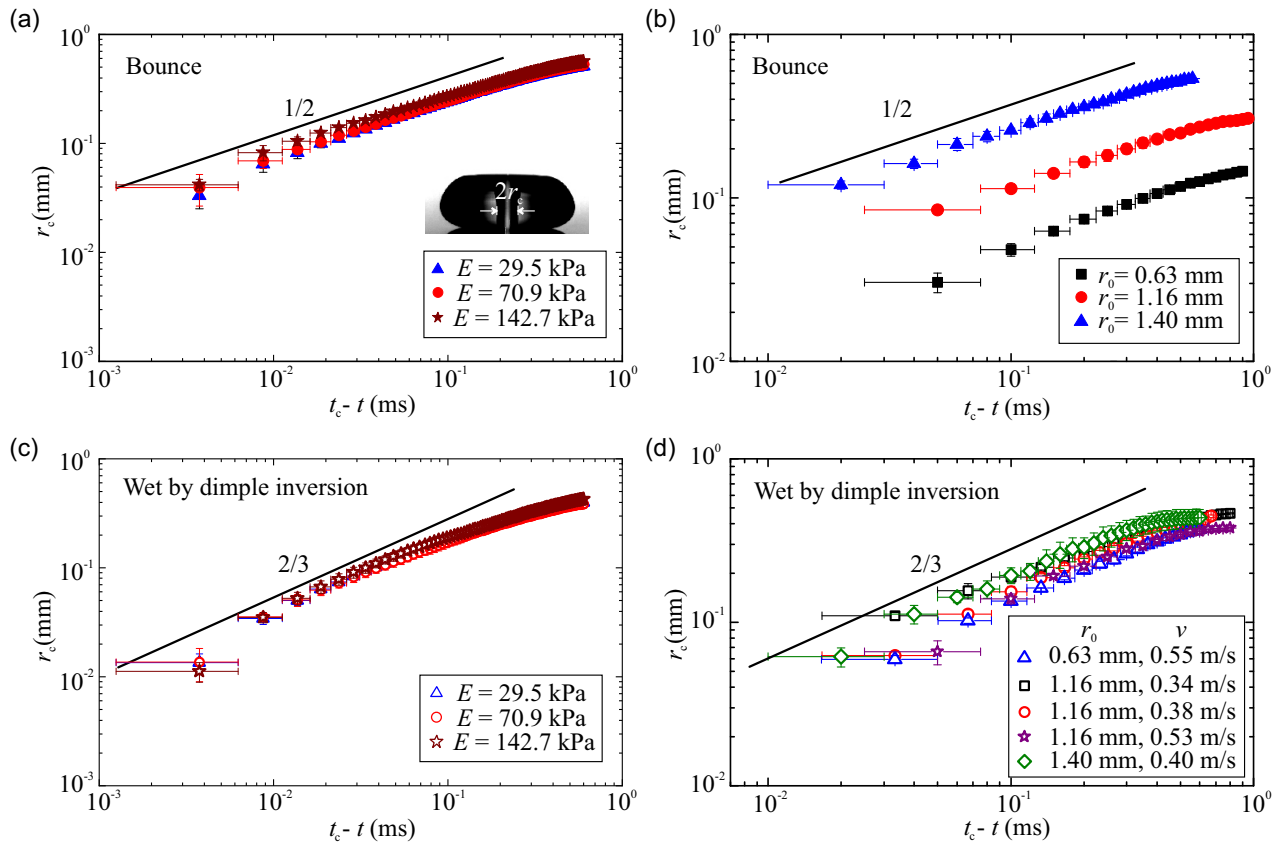


Fig. 6 (Color online) Plots showing the dependence of air cavity radius r_c with $t_c - t$ for different impact outcomes, i.e., bounce or wet, and different experimental parameters: (a) droplets bounce, $r_0 = 1.4$ mm, $v = 0.36$ ms $^{-1}$, varying E ; (b) droplets bounce, $E = 4.8$ kPa, $We \approx 2$, varying r_0 ; (c) droplets wet the solid by dimple inversion, $r_0 = 1.4$ mm, $v = 0.39$ ms $^{-1}$, varying E ; (d) droplet wet the solid by dimple inversion, $E = 4.8$ kPa, varying both r_0 and impact velocity v .

film and subsequently ruptures the air film. This behaviour is in a stark contrast to wetting initiation caused by random air film rupture commonly witnessed^{6,16}. We then constructed a bouncing-to-wetting phase diagram based on the observed air film rupture dynamics. We experimentally confirmed that for impact of water droplets on soft surfaces, bouncing-to-wetting transition is determined by interactions between the air cavity in the bulk and the air film trapped beneath the droplets, the so-called dimple inversion phenomenon. The stiffness of the substrates, on the other hand, does not significantly alter the bouncing-to-wetting transition. We have also found that, rupture of the air film by dimple inversion, in-turn, pins the base of the retracting bulk cavity to the surface and influences its collapsing dynamics. In such scenarios, the collapsing radius exhibits self-similarity and obeys a $2/3$ power-law in time, similar to the inertia-capillary break-away of a tapered fluid sheet³⁰ or other self-similar phenomena observed in free surface flows^{23,31}. For such collapsing mechanism, we further observed that the lower half of the collapsed air cavity causes entrapment and formation of an air bubble, while the upper half induces a liquid jet with velocity which can be as high as 100 folds of the impact velocity.

We highlight that within the tested velocity range, dimple inversion and its subsequent rupture causes wetting initiation at the center, as opposed to random rupture locations^{6,16}. This mode of

liquid-solid contact is a more controlled event where the liquid-solid footprint radius expands in a radially symmetric manner, similar to onset of quasi-static spreading of liquid drops on surfaces^{32,33}. Such controlled wetting characteristics may contribute to minimizing air bubble entrapment upon droplet impact and thus would be helpful in applications such as droplet deposition¹⁰ or ink-jet printing¹¹.

Conflicts of interest

There are no conflicts to declare.

Acknowledgments

The authors thank Maurice H. W. Hendrix for valuable discussions regarding the procedure to extract dimple profile shape from interference fringes. The authors also thank Marcus Lin for his help with rheometer measurements of the soft surfaces. This study is supported by Nanyang Technological University (NTU) and A*STAR (SERC Grant No. 1523700102). S.M. is supported by NTU Research Scholarship.

Notes and references

- 1 L. Xu, W. W. Zhang and S. R. Nagel, *Phys. Rev. Lett.*, 2005, **94**, 184505.

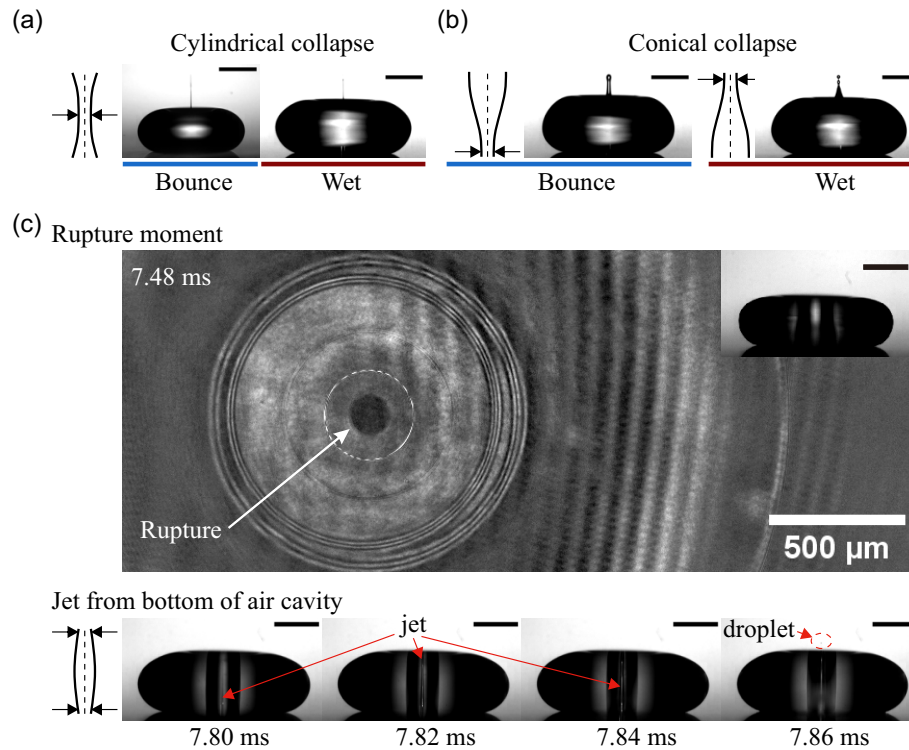


Fig. 7 (a) Snapshots showing the jetting dynamics by air cavity collapsing at its waist. Parameters: for the left snapshot (bounce), $E = 4.8 \text{ kPa}$, $v = 0.34 \text{ ms}^{-1}$, $r_0 = 1.16 \text{ mm}$; for the right snapshot (wet), $E = 70.9 \text{ kPa}$, $v = 0.38 \text{ ms}^{-1}$, $r_0 = 1.4 \text{ mm}$. (b) Snapshots showing the jetting dynamics by air cavity collapsing at its ends, i.e., bottom end, top end or both. Parameters: for the left snapshot (bounce), $E = 70.9 \text{ kPa}$, $v = 0.36 \text{ ms}^{-1}$, $r_0 = 1.4 \text{ mm}$; for the right snapshot (wet) $E = 29.5 \text{ kPa}$, $v = 0.45 \text{ ms}^{-1}$, $r_0 = 1.4 \text{ mm}$; (c) Snapshots showing the rupture moment by dimple inversion (upper panel) and the subsequent high-speed jet (lower panel) of a special case in which the jet originates from the bottom of the air cavity. This suggests that the high-speed jet originating from the bottom of the air cavity directly relates to dimple inversion phenomenon. At the time the jet appears in the air cavity, i.e., at $t = 7.8 \text{ ms}$, the liquid already wets all the impact area (snapshots not shown here). Parameters: $E = 4.8 \text{ kPa}$, $v = 0.47 \text{ ms}^{-1}$, $r_0 = 1.4 \text{ mm}$. The scale bars in all the side-view snapshots represent 1 mm.

- 2 M. M. Driscoll and S. R. Nagel, *Phys. Rev. Lett.*, 2011, **107**, 154502.
- 3 J. M. Kolinski, S. M. Rubinstein, S. Mandre, M. P. Brenner, D. A. Weitz and L. Mahadevan, *Phys. Rev. Lett.*, 2012, **108**, 074503.
- 4 J. de Ruiter, J. M. Oh, D. van den Ende and F. Mugele, *Phys. Rev. Lett.*, 2012, **108**, 074505.
- 5 J. de Ruiter, R. Lagraauw, D. van den Ende and F. Mugele, *Nat. Phys.*, 2015, **11**, 48.
- 6 J. de Ruiter, D. van den Ende and F. Mugele, *Phys. Fluids*, 2015, **27**, 012105.
- 7 R. C. van der Veen, T. Tran, D. Lohse and C. Sun, *Phys. Rev. E*, 2012, **85**, 026315.
- 8 A. L. Yarin, *Annu. Rev. Fluid Mech.*, 2006, **38**, 159–192.
- 9 B. Bhushan and Y. C. Jung, *Prog. Mater. Sci.*, 2011, **56**, 1–108.
- 10 J. Breitenbach, I. V. Roisman and C. Tropea, *Exp. Fluids*, 2018, **59**, 55.
- 11 N. Ashgriz, *Handbook of Atomization and Sprays: Theory and Applications*, Springer Science & Business Media, 2011.
- 12 E. Li and S. T. Thoroddsen, *J. Fluid Mech.*, 2015, **780**, 636–648.
- 13 E. Klaseboer, R. Manica and D. Y. Chan, *Phys. Rev. Lett.*, 2014, **113**, 194501.
- 14 L. Chen, J. Wu, Z. Li and S. Yao, *Colloids Surf. A*, 2011, **384**, 726–732.
- 15 L. Chen, E. Bonaccorso, P. Deng and H. Zhang, *Phys. Rev. E*, 2016, **94**, 063117.
- 16 K. Langley, A. A. Castrejon-Pita and S. T. Thoroddsen, *Soft Matter*, 2020.
- 17 B. Andreotti and J. H. Snoeijer, *Annu. Rev. Fluid Mech.*, 2020, **52**, 285–308.
- 18 D. Bartolo, C. Josserand and D. Bonn, *Phys. Rev. Lett.*, 2006, **96**, 124501.
- 19 L. Chen, L. Li, Z. Li and K. Zhang, *Langmuir*, 2017, **33**, 7225–7230.
- 20 M. H. Hendrix, R. Manica, E. Klaseboer, D. Y. Chan and C.-D. Ohl, *Phys. Rev. Lett.*, 2012, **108**, 247803.
- 21 M. Y. Pack, A. Yang, A. Perazzo, B. Qin and H. A. Stone, *Phys. Rev. Fluids*, 2019, **4**, 123603.
- 22 M. S. Plesset and A. Prosperetti, *Annu. Rev. Fluid Mech.*, 1977, **9**, 145–185.
- 23 R. F. Day, E. J. Hinch and J. R. Lister, *Phys. Rev. Lett.*, 1998, **80**, 704.
- 24 D. Leppinen and J. R. Lister, *Phys. Fluids*, 2003, **15**, 568–578.
- 25 R. Cox, *J. Fluid Mech.*, 1986, **168**, 169–194.

- 26 Q. Vo and T. Tran, *arXiv preprint arXiv:2101.02821*, 2021.
- 27 J. Guo, S. Zou, S. Lin, B. Zhao, X. Deng and L. Chen, *Phys. Fluids*, 2020, **32**, 122112.
- 28 A. U. Siddique, M. Trimble, F. Zhao, M. M. Weislogel and H. Tan, *Phys. Rev. Fluids*, 2020, **5**, 063606.
- 29 K. Yamamoto, M. Motosuke and S. Ogata, *Appl. Phys. Lett.*, 2018, **112**, 093701.
- 30 J. B. Keller and M. J. Miksis, *SIAM J. Appl. Math.*, 1983, **43**, 268–277.
- 31 J. R. Lister and H. A. Stone, *Phys. Fluids*, 1998, **10**, 2758–2764.
- 32 A.-L. Bianche, C. Clanet and D. Quéré, *Phys. Rev. E*, 2004, **69**, 016301.
- 33 S. Mitra and S. K. Mitra, *Langmuir*, 2016, **32**, 8843–8848.